Methods 60 (2013) 214–224

Contents lists available at SciVerse ScienceDirect

Methods

journal homepage: www.elsevier.com/locate/ymeth

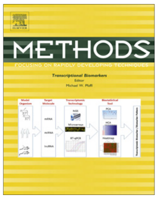

Brownian nanoimaging of interface dynamics and ligand–receptor binding at cell surfaces in 3-D

Igor R. Kuznetsov [a,b], Evan A. Evans [a,b,*]

[a] Biomedical Engineering, Boston University, Boston, MA 02215, United States
[b] Mechanical Engineering and Materials Science, Duke University, Durham, NC 27705, United States

ARTICLE INFO

Article history:
Available online 30 April 2013

Keywords:
Brownian particle imaging
Surface steric topography
Ligand–receptor binding kinetics
Nanoscale tracking in 3D
Off-line super resolution
Fast telemetry of receptor binding
Optical tweezers

ABSTRACT

We describe a method for nanoimaging interfacial dynamics and ligand–receptor binding at surfaces of live cells in 3-D. The imaging probe is a 1-μm diameter glass bead confined by a soft laser trap to create a "cloud" of fluctuating states. Using a facile on-line method of video image analysis, the probe displacements are reported at ~10 ms intervals with bare precisions (±SD) of 4–6 nm along the optical axis (elevation) and 2 nm in the transverse directions. We demonstrate how the Brownian distributions are analyzed to characterize the free energy potential of each small probe in 3-D taking into account the blur effect of its motions during CCD image capture. Then, using the approach to image interactions of a labeled probe with lamellae of leukocytic cells spreading on cover-glass substrates, we show that deformations of the soft distribution in probe elevations provide both a sensitive long-range sensor for defining the steric topography of a cell lamella and a fast telemetry for reporting rare events of probe binding with its surface receptors. Invoking established principles of Brownian physics and statistical thermodynamics, we describe an off-line method of super resolution that improves precision of probe separations from a non-reactive steric boundary to ~1 nm.

1. Introduction

After almost four centuries of effort, a common aim in microscope design remains to image cell structure with better and better spatial resolution while avoiding fixation and minimizing the effects of chemical labeling as much as possible. Not only transparent to visible light, isolated cells from animal tissues are typically soft dynamic structures that are very deformable and usually active when plated on a microscope cover glass. Because of the nearly chaotic motions of molecular scale cytoplasmic components, temporal resolution is also now recognized to be important in modern quantitative imaging. Even so, imaging modalities in studies of cell function and properties continue to evolve along an extremely challenging path guided for the most part by the quest to overcome limitations of resolution in light microscopy (i.e. nominally half the illuminating wavelength λ of visible light, ~½ × 500 nm). Although limited to some extent in temporal and/or spatial precision as well as encumbered by the need to add fluorescent labels, several notable advances in cell imaging have emerged from this quest [1] (e.g. stochastic optical reconstruction microscopy STORM, multi-color fluorescence and fluorescence-speckle microscopy FSM, stimulated emission depletion microscopy STEAD, advanced applications of fluorescence energy transfer FRET and evanescent field imaging).

By comparison, an equally prominent quest in single molecule biophysics has been to achieve fast nanometer precision in 1-D using tactile probes to test purified or recombinant constructs of molecules important in cell function [2] (e.g. molecular motors, mechanical enzymes, structural proteins, receptors and their ligands). Although nanometer or better in precision and well-resolved in time, these single molecule experiments are nearly always ex-vivo, i.e. lacking the complex chemical feedback from a living cell environment. Even though encumbered in some way, the impressive advances in both whole cell imaging [1] and single molecule probe experiments [2] continue to contribute exceptionally valuable insights into the biology, physics, and chemistry of cells that are unattainable by other approaches. Yet, except for examining the important kinematics of mobile constituents, less well developed by comparison are methods for imaging the surface of a live cell in a non-perturbing manner that can reveal dynamical properties of its interfacial structure and receptor interactions on the nanometer scale in 3-D with millisecond time resolution.

Abbreviations: VLA-4, very late antigen-4; CD49d/CD29, $\alpha_4\beta_1$-integrin; FN296, a recombinant construct of fibronectin type III repeats [domains 8-10 plus domains 12-14 including the alternatively-spliced CS-1 domain] available commercially as RetroNectin (Takara Bio USA); OT, optical trap; SD, standard deviation; MLE, maximum likelihood estimation; pdf, probability density function.

[*] Corresponding author.

E-mail address: evanse@bu.edu (E.A. Evans).

1046-2023/$ - see front matter © 2013 Elsevier Inc. All rights reserved.
http://dx.doi.org/10.1016/j.ymeth.2013.03.038

Although still very much a work in progress, the purpose of this methods article is to demonstrate an approach that comes close to achieving these design objectives.

Multi-scale in time and distance, the challenge has been to establish a sufficiently sensitive and stealthy sensor capable of nanoimaging the soft periphery of a cell and to report the unexpected dynamics involved in forming/dissociating ligand-receptor bonds on the ms-time scale. As illustrated in Figs. 1 and 2, studying these dynamics on the top surface of a spreading cell lamella is made even more complex due to the moving and irregular surface topography, which is modulated by hidden chemical signals from inside the cell. Moreover, the binding sites for ligation may be accessible one moment and restricted the next due to changes in integrin conformation or cytoskeletal (tectonic) displacements. Extending the well-known 2-D dynamics explored at cell surfaces with optical traps [3,4] to 3-D, we have developed an OT imaging system to meet this challenge that continues to report transverse displacements of the probe with nm precision yet shifts the emphasis to tracking displacements of the probe normal to the cell surface with comparable precision. Imaging dorsal surfaces of cell lamellae with passivated and ligand-conjugated beads (Fig. 1), we demonstrate that the approach provides a sensitive long-range (~30–50 nm distant) sensor for defining the steric topography of a lamella with a bare precision of ~5 nm and, at the same time, a fast telemetry (~0.01 s) for reporting rare events of receptor binding/release as well as the subsurface cytoskeletal reactions to binding. Utilizing principles of Brownian physics and statistical thermodynamics, we describe off-line methods of super resolution that can significantly improve precision of both the surface elevation and relative location of a site of ligand–receptor binding above the surface.

2. Design overview and rationale

Described in detail in the following sections, the core of the nanoimaging system is a 1-µm glass sphere held and levitated above a coverglass substrate by a near-infrared (1064 nm) laser optical trap. Illustrated schematically in Fig. 1A, cell targets are plated on a protein-coated coverglass in a microscope chamber. Maneuvered through a specially designed LabVIEW (National Instruments) interface and a 3-axis linear piezo-driven stage, a target cell lamella is positioned underneath the levitated probe with nanometer precision. A high-speed CCD video image processing system is interfaced with the computer software to track the micron-size probe (cf. Fig. 1B) in 3D on-line at ~100 frames/s during the course of computer-directed vertical and lateral movements of a cell by the piezo stage. Lateral tracking of the probe follows the method for image analysis developed in our previous studies of single molecule interactions [5,6], yielding precisions of ±2 nm SD. However, unlike tracking the larger 3–4 µm spheres used in our previous approach, here we have chosen 1 µm size spheres to minimize probe-surface contact while still maintaining a well-configured trapping potential. Because the probe is only two wavelengths of light in diameter, it was necessary to establish a new on-line method for tracking the small probe along the optical axis. As we show later, the software developed for height tracking provides a bare precision of ±4–6 nm SD over a span of 200–300 nm in probe elevation without retarding the video framing rate. As described in Section 4.3, the lamella of a cell spreading below the levitated bead is subjected to an initialization cycle that raises/lowers the lamella surface to establish its reference separation from the trap center. For simple imaging, the lamella is then translated laterally relative to a passivated probe to scan its topography over a long traverse (the first live cell demonstration appearing in Section 5) or, alternatively, kept stationary to report local changes in topography over time driven by cytoskeletal dynamics.

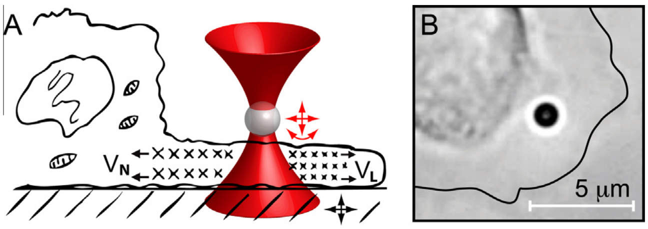

Fig. 1. (A) Schematic of the imaging probe confined in a laser optical trap and positioned to interact with the dorsal surface of a spreading cell lamella. The black arrows symbolize controlled movements of the 3D stage. The red arrows symbolize thermal motions of the bead inside the trap, random translational and rotational displacements. The interior cross-hatched components represent the active F-actin network, moving rearward toward the cell body (velocity v_N) and rapidly assembled at the advancing edge of a lamella (velocity v_L). (B) Transmitted visible light image of a 1 µm diameter glass probe positioned above the lamella of a spreading leukocytic cell (the lamella boundary has been traced to enhance visibility).

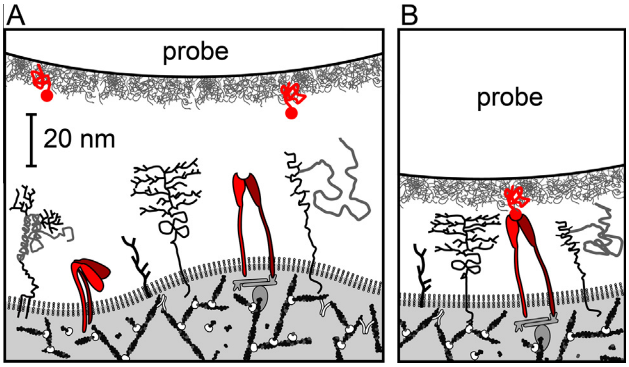

Fig. 2. Schematic of the "attoliter" Brownian interaction region explored by probe ligands and cell receptors when forming bonds close to a lamella surface. (A) Sketched to match the sizes expected for components, the molecular roughness of an alkoxysilane coating on the probe bead (upper surface) appears in gray along with dilute chemically-linked protein ligands in red. Facing the probe from below, and anchored to the cell plasma membrane bilayer (gray zipper), is the membrane superstructure containing heterodimeric integrin receptors in dark red interspersed amongst constituents of the glycocalyx in gray. Beneath the lipid bilayer is the active F-actin cytoskeleton in black that drives cell motility and dynamic displacements in the surface topography. (B) Schematic of a probe ligand bound to a cell surface integrin. Note: inactive and active states of integrin heterodimers are symbolized by bent and extended conformers respectively.

Much more involved is the methodology for analyzing the kinematics of the lamella surface and a site of ligand–receptor binding during a brief period of ligation (the second live cell demonstration in Section 5). Indicative of the complexity, the panels in Fig. 2 illustrate the putative molecular architectures regulating ligation drawn on a scale matching the probe. The molecular reactants, probe ligands and cell integrin receptors, are colored red. The main contributors to sterics, the probe PEG-silane and the lamella surface glycocalyx, are shown in grey. Also idealized is the irregular topography expected for a plasma membrane surface. Ligation events arise unexpectedly at random times when a rare thermal fluctuation of the probe drives the coating into contact with the lamella glycocalyx enabling a bond to form (cf. Fig. 2B). Idealized conceptually, the repeated close encounters of a probe and cell surfaces create a fluctuating "atto-liter volume" in which ligand-receptor bonds occasionally form [note: $1\ \text{L} = 10^{24}\ \text{nm}^3$]. The size of this miniscule reaction space is defined by the extent of probe-glycocalyx overlap δ (~5–10 nm) and the associated area of interfacial contact $2\pi\ R_s\ \delta$ ($\sim 3000 \times 5\text{–}10\ \text{nm}^2$). Although sketched as naïve caricatures, all of the components in Fig. 2 can be expected to affect the likelihood that a close encounter produces a binding event. Intuitively, one expects receptors hidden in the membrane valleys and/or present as inactive folded states to remain unbound; only those exposed above the glycocalyx, perhaps on top of membrane promontories, are likely to form bonds. Yet, more subtle is that rare thermal fluctuations can drive probe ligand components into the cell glycocalyx, initiating a binding event. By imaging such events with a weakly-trapped probe, we will demonstrate off-line methods to significantly improve definition of binding site movements relative to the lamella surface. In doing so, we need to consider two physical consequences of the substrate (lamella or inert) boundary – one thermodynamic, determined by the divergent repulsion of the probe by the boundary, and the other dynamic, arising from the divergent damping of the probe close to the boundary.

3. Instrument

3.1. Layout

Outlined here is the instrument used to image the nanoscale dynamics in 3-D of a 1-μm probe interacting with a soft sticky surface under ultra-low impingement forces (~fN). In the next section, we illustrate the approaches developed for on-line tracking of the probe, which yield position data at ~100 Hz with precisions of ±4–6 nm (SD) in the vertical direction and ±2 nm (SD) in the transverse directions. We then describe the methods for referencing the cell surface distance to the trap center and the off-line MLE analysis that enables super-resolution of the bare vertical height tracking of substrate elevation. Removing the random errors in bare tracking and correcting for the CCD camera integration time, we demonstrate how to quantify the trapping potential (spring constants) in 3D and how to independently specify elevations of a receptor-ligand binding site relative to the lamella interfacial boundary.

Fig. 3 is a schematic of the instrumentation used to configure the laser trap. Creating the trap is optically focused light from a stable 500 mW Nd:YAG 1064 nm CW diode laser (Compass 1064–500, Coherent Inc., Santa Clara, CA). The laser beam is passed first through a liquid crystal power controller (Brockton Electro-Optics Corp., Brockton, MA), then a beam expander (2–8×, Special Optics, Wharton, NJ), and finally is focused by the 100x/1.30NA oil immersion objective (Carl Zeiss, Inc., Thornwood, NY) of a Zeiss Axiovert S100 inverted microscope. All optical components have been coated for optimal transmission at the laser wavelength of 1064 nm. Programmed by the operator, the computer station controls the laser power and the position of the stage as well as collects and analyzes the image data from CCD camera in real time. Illuminated by a 100 W halogen lamp, a bright field image of the probe is formed using the trapping objective and captured by a cooled (−15 °C), 12 bit CCD camera (SensiCam, Cooke Corp., Auburn Hills, MI). A closed-loop, 3D piezo-controlled microscope stage (P-517.3 CD, PI, Auburn, MA) is used to position and displace the sample chamber with respect to the objective (and the optical trap) with sub-nm precision. When operated in the fast frame mode, the camera framing rate depends on the number of the image lines collected. Tracking the 1-μm probe at 100× magnification in three dimensions requires a field of ~100 lines, reducing the framing rate to about 100 frames per second. The software components for stage position control, bead tracking and analysis have been implemented in LabVIEW 6.5 (National Instruments Corp., Austin, TX).

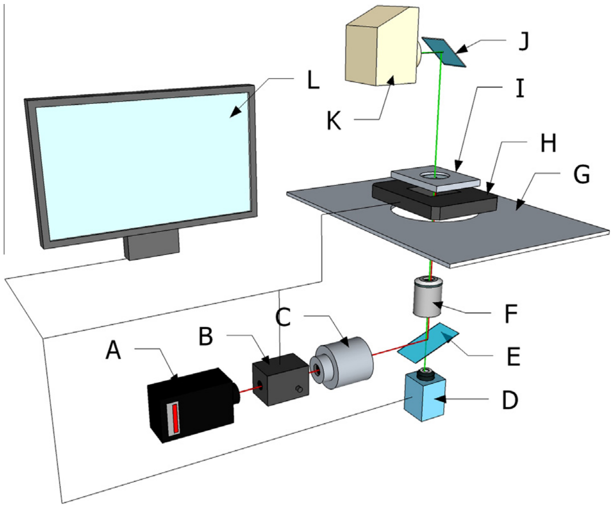

Fig. 3. Schematic layout of the instrument used for probe imaging and stage manipulation in 3D. (A) Laser head, (B) power controller, (C) beam expander, (D) Sensicam CCD camera, (E) beam splitter, (F) microscope objective, (G) microscope stage, (H) 3D positioning stage, (I) microscope chamber, (J) mirror, (K) halogen lamp, and (L) computer interface.

3.2. Probe preparation

Base-cleaned borosilicate glass microspheres (Duke Scientific, Palo Alto, CA) are conjugated with reactive mercapto- or amino-trimethoxysilanes (United Chemical Technologies, Bristol, PA) before use as probes. For imaging cell-surface topography, the silanized beads are then passivated either by a binding maleimide- or NHS- PEG2000 to the appropriate silane reactive group or by directly linking a non-specific protein (e.g. albumin) to the reactive group. For imaging receptor binding events and cell signaling dynamics, the silanized glass beads are first reacted with a mixture of a maleimide- or NHS- PEG2000 plus the hetero-bifunctional malemeide-PEG3500-NHS (Shearwater Polymers) terminated by covalent capture of a specific protein ligand. Selected from a broad distribution of diameters (~1–2 μm), spheres for use as probes are chosen simply by having an apparent diameter (2R) close to 1 μm based on prior calibration of the image scale factors. Although varying by 0.1 μm, the trapping potential for each sphere can be calibrated prior to its use by the nanoimaging system obviating the need for accurate specification of its diameter.

4. Imaging sensor

We have established robust tracking algorithms that facilitate fast processing of the probe lateral and height displacements within the CCD frame capture time. In tracking movements of spheres with diameters (2R) close to the wavelength of visible light (~0.4–1.5 μm) along the optical axis, we are not able to employ methods normally used for either much larger beads (e.g. interferometric or focus-transfer function analyses) or much smaller beads (e.g. point-spread function analysis). Thus, to track probe height, we have devised a phenomenological metric for accurately quantifying changes in its focus contrast over a large span of height.

4.1. Probe tracking and distance calibrations

For each image captured by the CCD camera, the tracking software follows a sequence of first lateral then vertical position analysis. The first step is to establish the center position of the probe (X,Y). Initially, the position (to within one screen pixel) is defined by the center of mass of the image intensity gradient map. The center of mass position is then refined (to within a random error of ±2 nm SD for a stationary bead) using a normalized cross-correlation based on mirror images [5]. Calibration of the length scale for displacements in the lateral plane is provided by imaging a standardized micrometer grid over a large distance and determining the number of screen pixels per nanometer. Once the center position is determined, it defines the origin of the vertical (optical) axis in the second step of establishing the probe elevation. Calibration of height tracking in the vertical direction is achieved by correlating a focus-dependent metric for the probe-image radius (Fig. 4.1A–B) to linear up/down movements of the piezo-driven stage relative to the objective focal plane (Fig. 4.1C,D). When imaging a cell lamella, the span of probe heights needed to be tracked lies well within the linear range (~200–300 nm) revealed by this phenomenological algorithm (Fig. 4.1D). The bare measurement error in height tracking (±4–6 nm SD) has been determined using immobilized probe spheres attached to the coverglass and moved up/down slowly at ~100 nm/s (Fig. 4.1C). As we discuss in Section 4.3 below, faster movements (e.g. Brownian displacements in the optical trap) become blurred during the time needed for the CCD to capture the image. Thus, the effects of both motion blur and random measurement error must be taken into consideration in order to optimize precision in position tracking. [Note: all of the data described in this article were obtained in high salt buffers (150 mM NaCl plus Hepes) with an exponential screening length for electrostatic interactions <1 nm. Also, exposed regions of bare glass on the probe and coverglass were passivated by washing the surfaces in salt buffers with a small concentration of fatty-acid free bovine serum albumin ~10^{-3} g/ml.]

Levitated in a soft optical trap, probe heights become broadly distributed relative to the hidden equilibrium position defining the trap center above the substrate surface. To determine and calibrate the separation between the probe and substrate surfaces, we use the diffuse Brownian "cloud" of vertical positions as a tactile long-range sensor for detecting contact with a steric boundary (e.g. the cover glass or a cell lamella). Raising/lowering the piezo stage as demonstrated in Fig. 4.2 establishes a bare reference for the intervening separation between a probe and the surface prior to commencing an imaging protocol. We show below how this initialization cycle is also used to calibrate the trapping potential confining a probe particle.

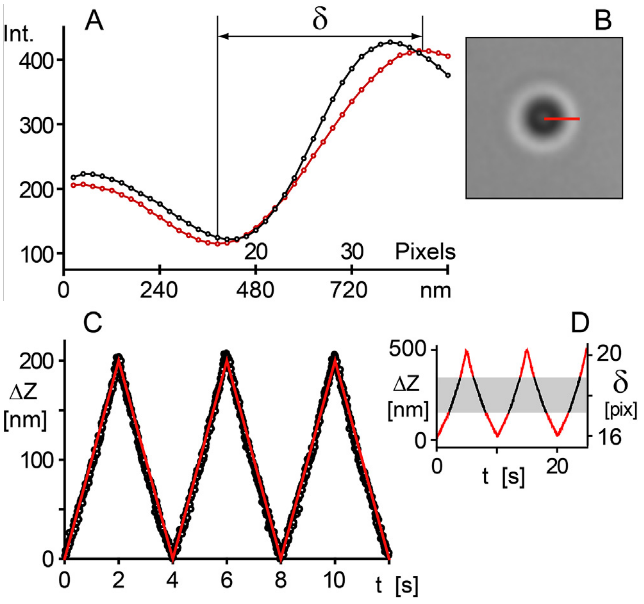

Fig. 4.1. (A) Angle-averaged radial intensity profiles of an immobilized probe (image in B). The black and red curves in A are the intensity profiles of images taken at two vertical stage positions 500 nm apart as set by the piezo stage with sub-nanometer precision. Defined by the parameter δ, the metric for change in probe focus is taken as the distance between the intensity maximum and minimum, which ranges from 16 to 21 pixels over 500 nm displacements in A. Restricting the stage movement to a 200 nm span in C, the focusing metric is demonstrated to map linearly onto the stage movement. The coefficient of proportionality provides the conversion factor relating changes in δ to changes in probe height. Moving the stage up and down over a larger span of 500 nm in D, the correlation begins to deviate weakly from linearity beyond ~250 nm. Exploring elevations in the 200–250 nm range at ~100 nm/s yields a bare vertical precision in height tracking of ±4–6 nm SD.

4.2. Levitated probes and calibration of Brownian distributions in 3-D

When levitated in a soft trap, probe positions fluctuate rapidly in time, which blurs the probe image during capture by the CCD. The impact of blur depends on the ratio α of image capture time τ_{CCD} to the characteristic relaxation time τ_{OT} for Brownian displacements in the trap, i.e. $\alpha \equiv \tau_{CCD}/\tau_{OT}$. Because lateral trapping is much stronger than vertical trapping, relaxation in the trap differs significantly in time between the lateral and vertical directions. Moreover, because of long-range hydrodynamic coupling to the substrate, the relaxation times increase dramatically close to the surface when distances are less than 0.1 of the probe radius. Yet when further from the surface (e.g. >100 nm), blur of probe motions in the trap become pronounced, which is also where the trap potential is best calibrated. By comparison, when nanoimaging of surfaces at distances of 50 nm or less, the impact of blur on height traces is suppressed by the damping and the free probe heights become essentially limited by the tracking error for immobilized probes. In a later section, we will use results from a Brownian simulation to demonstrate this near-perfect fidelity in height statistics close to a surface and the benefit of hydrodynamic retardation. While ~100 fps is perfectly adequate for imaging heights close to a non-reactive surface, we demonstrate in the final section that the primary benefit of faster framing rates would be to significantly increase the statistics during brief periods of probe binding to a cell surface in order to improve the super resolution of cell surface and binding site locations.

4.2.1. Brownian image of the trap potential in 3-D

As demonstrated in Fig. 4.3A, we employ bare on-line tracking to obtain an image of the trap potential in 3D and then derive the true trap potential (transverse and vertical spring constants) using an analytical expression to correct for image blur [7]. Not only needed to determine forces applied to the probe, imaging the trap potential in 3-D can also verify the Brownian physics expected for free probe motions and provides a way to correct for the inability to capture fast particle movements with an imaging system. Because large displacements of a probe in the trap are dri-

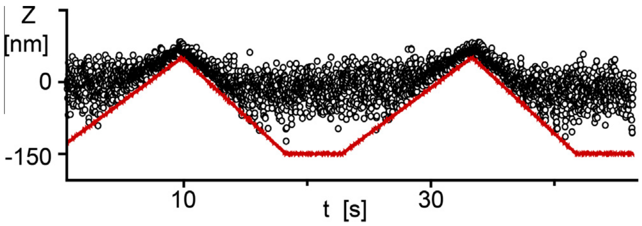

Fig. 4.2. Referencing separations between substrate and probe surfaces to the equilibrium position in the trap. When levitated above a surface in a trap, the procedure for determining the relative distance between the probe and substrate surfaces involves a programmed initialization cycle of up-down movement of the piezo stage, which pushes the probe up/down relative to the trap center. Matching the piezo-stage trajectory (red line in Fig. 4.2) to the indented profile of the Brownian height fluctuations (black circles) provides the bare height reference for the substrate surface relative to the trap center. The height referencing enables subsequent changes in surface separation to be defined relative to any piezo trajectory.

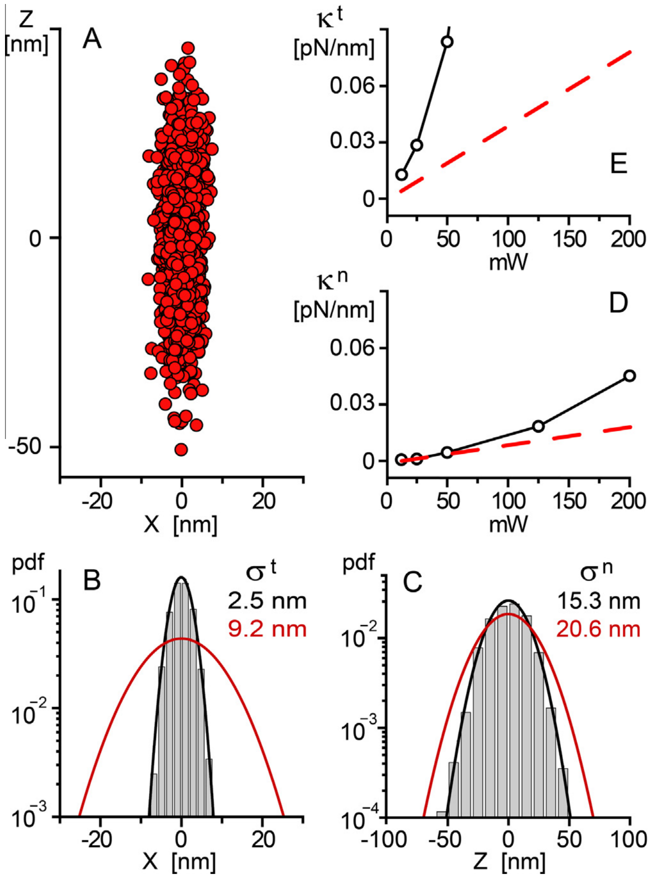

Fig. 4.3. Image of the free energy potential created by the optical trap confining a 1 μm glass probe at a mean distance 150 nm above a substrate. (A) Bare positions of the probe obtained at a power of 125 mW are shown overlaid in the XZ plane. Tracked for 20 s at ~100 fps and collapsed onto the XZ plane, the 3D distribution of bare probe positions reveals a distinct cigar-like confinement potential – albeit "cropped" all-around significantly by blurring. (B,C) Histograms of the observed positions in X and Z respectively plotted on $\log_{10}$ scale to demonstrate the harmonic character of the trapping potential. Superposed on each histogram are two Gaussian probability distributions, again plotted on $\log_{10}$ scale: Black curves are MLE fits yielding the observed SD^2. Red curves are distributions predicted by the blur-corrected spring constants κ_{OT}. The intervening gaps between red and black distributions reveal the major difference in band width between each "low-pass" filter. (D, E) Spring constants in vertical and transverse directions are shown for a range of laser power from 12.5 to 200 mW. Circles are the apparent spring constants based on the observed variances in probe imaging traces corrected for random tracking errors. The red dotted lines show the linear correlations of blur and tracking error-corrected spring constants as functions of laser power.

ven to recoil rapidly, CCD integration acts like a "low pass" spatial filter suppressing detection of the large fluctuations. Even though blurred most in the transverse dimension, both the transverse and vertical distributions of free probe positions in the image traces are perfectly Gaussian as shown by matching upside-down parabolas to the distributions plotted on a log scale as in panels B–C of Fig. 4.3. Corrected for both motion blur and random tracking error, the overlaid (red) continuous pdf curves reveal the transverse and vertical harmonic fields that actually confine the free probe displacements at a separation of ~150 nm from the surface. Thus, we can invoke Boltzmann's principle of equipartition of energy to determine the vertical and transverse spring constants using the variances that define the corrected distributions [i.e. variance the ratio of thermal energy to a spring constant, $\sigma^2_{OT} = k_BT/\kappa_{OT}$.

To determine the true trapping potential, the observed variances of vertical and transverse fluctuations obtained from imaging a free probe must be corrected for two factors: 1) image blur by CCD integration and 2) the random time-independent tracking error σ_{err}. For a soft trap positioned ⩾100 nm from a surface, the ratio of camera integration time to the characteristic relaxation time for probe movements in the trap ($\alpha \equiv \tau_{CCD}/\tau_{OT}$) is sufficient to correct motion blur. Since optical traps differ in strengths for transverse (t) and vertical (n) confinement, blur corrections involve two such ratios ($\alpha^{n,t} = \tau_{CCD}\kappa^{n,t}_{OT}/\zeta^{n,t}$). When the trap center ($z = 0$) is very far from a surface (separation $-z_w = \Delta_w > \mathrm{R}$), damping of a free probe in transverse and vertical directions both approach the value given by the Stokes drag $\zeta_\infty = 6\Pi\eta\,\mathrm{R}$ (aqueous viscosity). However, for separations $\Delta_w < R$ from a smooth substrate, vertical damping increases much more strongly with reduction in separation than transverse damping as shown by the following approximations $C^{n,t}_\zeta = \zeta^{n,t}/\zeta_\infty$ for the numerical factors [8]:

$$\begin{aligned} C^n_\zeta &\approx (R/\Delta_W) + 1 \\ C^t_\zeta &\approx 0.50\ln(R/\Delta_W) + 1.09 \end{aligned} \tag{4.1}$$

Note: the transverse damping factor is that for a "torque-free" sphere [9], thus combines the transverse force on a freely rotating sphere with the force for translation of a non-rotating sphere.

To calibrate the trapping potential for a particular probe (e.g. Fig. 4.3A), we first reference the substrate separation to the trap equilibrium position as illustrated in Fig. 4.2. Then fixing the substrate elevation, we image the trap as seen in Fig. 4.3A. Using the separation distance (e.g. $\Delta_w = 150$ nm in Fig. 4.3A) between the probe and substrate, we calculate the damping coefficients and solve a transcendental expression for each correction [7],

$$\left(\sigma^2_{obs} - \sigma^2_{err}\right)^{n,t} \approx \frac{2k_BT}{\alpha^{n,t}\kappa^{n,t}_{OT}}\left\{1 - \frac{1}{\alpha^{n,t}}\left[1 - \exp\left(-\alpha^{n,t}\right)\right]\right\} \tag{4.2}$$

to obtain the true vertical and transverse trap spring constants $\kappa^{n,t}_{OT}$. Since the tracking errors are random time-independent variables, we simply subtract the error variance from the observed variance prior to solving each equation numerically for the trapping constant κ_{OT}.

Applying this approach to the softer confinement of probe height fluctuations, we show in Fig. 4.3C that the true vertical trapping strength increases linearly with laser power as expected over the full range from 12.5 to 200 mW. However, because of much stronger confinement and much larger blur effects, it was only possible to determine true transverse trapping strengths and test the linear correlation up to laser powers of ~100 mW with a CCD integration time $\tau_{CCD} \approx 0.01$ s. Even so, the transverse trapping strength corrected for image blur also confirmed the linear response. Compared here with data up to 50 mW, the linear correlation in Fig. 4.3E has been extended to show the expected increase in transverse trapping strength up to 200 mW. Corrected for blur and tracking errors, the aspect ratio for the potential trapping a 1μm probe is found to be ~4–5:1.

4.2.2. Super-resolution and dynamic fidelity close to smooth surfaces

As described in 4.2.1, the viscous drag on a probe moving normal to a surface diverges at small separations ($\zeta^{\,n} \sim \mathrm{R}/\Delta_w$) thereby quenching the scale for velocity impulses. Thus, the relaxation time for free probe height fluctuations in an optical trap increases dramatically and images of the heights with a CCD camera are much less affected by blurring when close to a surface. If close enough, the camera integration time (exposure time) will fall below the probe relaxation time to yield fidelity in height statistics. Using the blur parameter α^n characterizing soft vertical confinement (4.2.1), the prediction to be verified below is that the blur effect demonstrated in Fig. 4.3 should disappear from height images when distances from a steric boundary are less than 75 nm and imaged at 50 mW laser power. Even though valid for a non-reactive surface, we show later that the expected fidelity no longer holds when the probe is bound to a cell surface. The combination of tight linkage of the probe to a cell surface receptor and the stiff surface repulsion completely overwhelm the weak trapping forces allowing only restricted movements and very small fluctuations. Still, the dynamic fidelity close to a steric boundary remains important in the determination of surface heights just before and after the binding event. For this reason, we have used a Smart Monte-Carlo (SMC) simulation to model probe height fluctuations close to a surface. The simulation employs a novel analytical expression for the Brownian propagator (a Green's function) that governs local Markovian equilibration of the distribution (details of the simulation to be published elsewhere). As shown in Fig. 4.4, results from the simulation support the use of a phenomenological relation to predict the crossover distance above which motion blur becomes significant.

The important steps needed to implement such a SMC simulation are first to define the thermodynamic limits predicting equilibrium positions of a probe in the trap throughout the course of programmed movements of the substrate. Referenced to an origin set by the equilibrium location of the trapped probe when far from the surface, statistical thermodynamics (Appendix A) predicts that the equilibrium position shifts progressively outward as the surface is moved closer to the unstressed origin of the trap minimum. Defined by the parameter *b*, the shift in equilibrium location is the consequence of entropy confinement as the fluctuation distribution is cut off by the boundary. The other important step is to specify the dynamic (time-dependent) Green's function describing the Markovian approach to local equilibrium in a space rescaled by the gradient in mobility. This propagator regulates the Brownian impulses contributed to the Langevin (Stokes) dynamics of the probe at each trial step [9]. The steric boundary condition is effectively implemented by divergence of the probe damping as positions approach the surface.

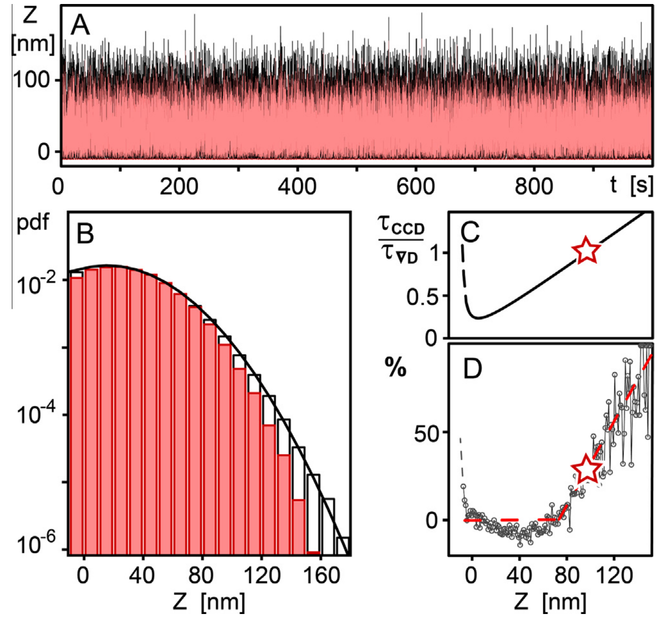

Fig. 4.4. (A) Simulation of height fluctuations for a 1 μm probe in an optical trap (50 mW) close to a surface (black trace) and the effect of CCD integration τ_{CCD} = 10 ms on position detection when imaged by the camera (pink trace). Hydrodynamic retardation of probe movements closer to the surface increases detection of positions when summed over a fixed window of time (with the notable exception of very close to the surface where mobility vanishes). (B) Fidelity of statistics sampled at 100 fps near a surface. The distributions are plotted on a log scale to amplify the statistics far from the surface and illustrate the modest impact of blur averaging until reaching large separations (>3 SD_{OT}). (C, D) Blurring (reduction in detection) emerges when the time scale τ_{CCD} for CCD integration exceeds the relaxation time characterizing probe equilibration. (C) Ratio of camera integration time τ_{CCD} to the time scale $\tau_{\nabla D}$ characterizing Markovian approach to local equilibrium in a medium rescaled by a gradient in mobility. (D) Fractional reduction in detection as a function of separation from the surface determined by the simulation. Open red stars identify the crossover distance at $\tau_{CCD}/\tau_{\nabla D}$ = 1.

We have used the analysis describing Markovian approach to local equilibrium in a space rescaled by a gradient in mobility to estimate a position-dependent relaxation time. By analogy to the blur parameter appearing in Eq. (4.2), we expect the following ratio of camera integration time to the position dependent relaxation time to correlate with the separation distance where blur effects become significant:

$$\tau_{CCD}/\tau_{\nabla D} \approx \frac{\tau_{CCD} D_\infty}{R}\left\{\frac{1}{4(z-z_w)} + \frac{\kappa_{OT}}{2k_B T}[3z - 2z_w - b]\right\} \tag{4.3}$$

Here, the probe-surface separations $(z - z_w)$ are defined by a steric boundary at $z_w = -10$ nm below the unstressed trap center at $z = 0$. The following parameters were used in the simulation: time step $\Delta t = 0.001$ s, $\kappa_{OT} = 0.003$ pN/nm, R = 500 nm, Stokes drag ς_∞ 10^{-5} pN-s/nm.

The effect of blurring was modeled by a sequential 10-point averaging. Hence, the blurred image contains 10 times fewer positions, each spread over $\Delta t^{blur} = 0.01$ s. Fig. 4.4B presents height positions and a MLE fit of the pdf for the full (white bins and black line) and blurred (pink bins) position traces.

4.3. Target positioning and super-resolution of surface referencing

4.3.1. Target positioning

Maneuvered using a custom-designed LabVIEW (National Instruments) interface and a 3-axis linear piezo-driven stage, a passive substrate or target cell lamella is positioned underneath the levitated probe bead with nm precision. The surface is first positioned well below the levitated probe and then returned to this elevation following an initialization cycle that raises/lowers the stage to establish the relative distance to the trap center.

4.3.2. Surface referencing and super-resolution

In the initialization cycle, the surface is raised to compress the soft underside of the Brownian distribution of probe heights and also deflect the probe upward. The surface is then lowered to allow these fluctuations to re-emerge as shown in Fig. 4.2. Matching the piezo trajectory to the profile of compressed positions, we establish a bare reference for the surface height relative to the trap center. In other words, the material surface (e.g. cover glass or cell lamella) is defined by a steric boundary that sharply terminates downward probe fluctuations. While nominally limited to a precision of ±4–6 nm, we have developed an off-line method to super resolve images of non-reactive boundaries to ~1–2 nm given sufficient statistics. In a live cell demonstration at the end, we show how super resolution of the steric boundary characterizing a lamella surface before – and – after a probe binding event can establish crucial references for dynamical movements of the binding site during the intervening period of ligation.

Here, we demonstrate the super resolution method using the image trace of a passivated probe positioned by a 50 mW trap above an albumin-coated cover glass substrate in 150 mM salt buffer. Fig. 4.5E shows a 25 s segment of the probe heights beginning with the probe equilibrated about 90 nm above the substrate for 10 s, followed by brief up/down cycle of displacement terminated at a bare reference elevation about 10 nm below the initial trap equilibrium position for the last 12 s. The programmed piezo trajectory is shown by the red line plotted in Fig. 4.5E. Probe heights and 3D position statistics are colored pink and blue for the two stationary substrate elevations, 0–10 s and 13–25 s, respectively. Plotted in Fig. 4.5A–D, are the distributions of transverse X–Y positions

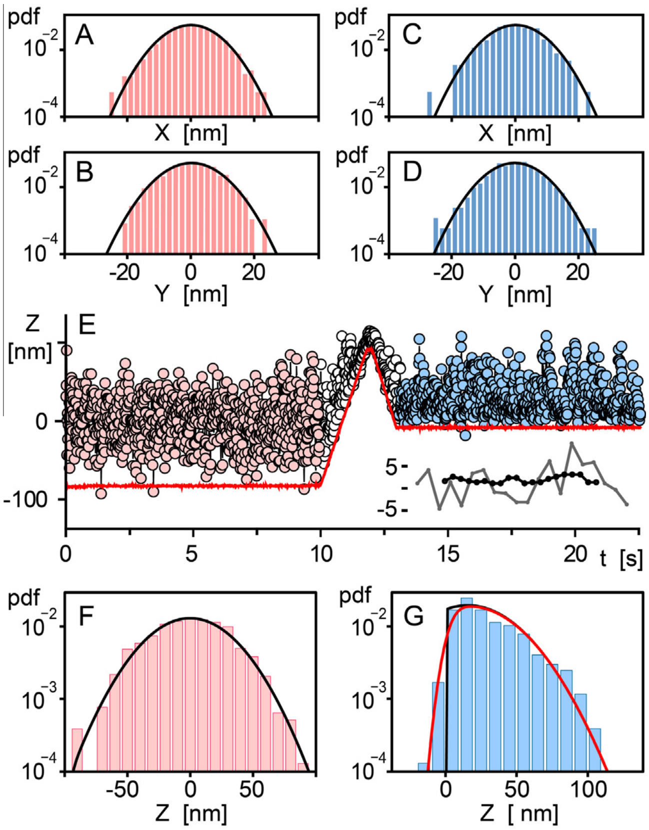

Fig. 4.5. Determination of probe heights relative to a steric substrate positioned at two bare elevations: ~100 nm and ~10 nm below the starting trap center. (A–B) Distributions of X–Y probe positions (±7.2 nm and ±7.7 nm SD respectively) collected at a distance of ~90 nm. (C–D) Distributions of X–Y probe positions (±7.25 nm and ±7.3 nm SD respectively) collected at a distance (MLE fit) of ~14 nm. Both distributions of X–Y positions are near perfect Gaussians (inverted parabolas on log scales) yet show frazzled peripheries etched away by blur effects. As shown by results Fig. 4.3, the actual transverse distributions are twofold broader (~15 nm SD) than revealed by tracking at 100 fps. (E) Probe heights imaged from 0 to 25 s and interrupted by an up/down movement of the substrate (red piezo-trajectory) terminating close to the initial trap center position at zero height. Probe position data prior to the up movement (<10 s) are colored pink and data after termination of the down movement (>13.2 s) are colored blue. (F–G) Distributions of probe heights at the initial and final stationary elevations plotted on log scales versus height relative to the initial trap center position ("zero"). The black line contours superposed on the distributions are the optimized MLE fits for the equilibrated thermodynamic distribution after deconvolution of the random errors in height tracking. Governed by two parameters, the free energy potential defining the thermodynamic trial distribution (cf. Appendix A) is a harmonic trapping potential (Gaussian with variable SD and center position) terminated by a steric barrier (sharp cut off at a variable position). Intersection of each black line contour with the height axis defines the super-resolved surface elevations. Convolved with the Gaussian distribution of height-tracking errors, the red-line contour in G shows the MLE match to all of the height statistics yielding the truncated thermodynamic distribution (black-line contour). The similar error-convolved MLE match to the height statistics in F differs imperceptibly from the black-line contour. Even though very different in appearance, the harmonic potentials determining the thermodynamic distributions in F,G have nearly identical stiffness (κ_{OT} = 0.0036 and 0.0039 pN/nm respectively). Most significant, the trap center and elevation of the steric boundary determined by MLE analysis in G are both shifted upward relative to the original trap center ($z = 0$): to 15.5 nm for the displaced trap minimum and to 1.4 nm for the super-resolved boundary. (E-insert) Shown in gray are MLE elevations estimated using 50 data points. The MLE elevations estimated using 250 data points are shown in black.

cumulated at each trap-substrate separation. Clearly evident, the data in A–B and C–D show nearly identical centro-symmetric confinement of the transverse fluctuations, even though obtained at 10-fold difference in trap-substrate separation. Consistent with the weak logarthmic dependence of damping on separation, the transverse distributions are little affected by the change in proximity to the surface and at the same time show no evidence of any adhesive interaction as expected for a non-sticky boundary. On the other hand, the strong encroachment towards the trap center significantly frustrates the height fluctuations, displacing the trap center (distribution peak) ~15 nm upward from its initial position. In order to critically examine the consequences of strong encroachment, we have super resolved the substrate position and location of the trap center. To do this, we have implemented an approach that involves a two-parameter fit of a trial function. Described in the section to follow, the fit is accomplished by minimizing a Hessian to find the Maximum Likelihood Estimate (MLE) optimizing the match to all the height positions. Applied to the compressed height fluctuations in Fig. 4.5E–G, the two-parameter MLE fit predicts the trap equilibrium position (peak of the probability density) at b = 15.5 nm, and the actual surface elevation at Z_W = 1.4 nm. Based on these values, the blur-corrected trap stiffness is calculated to be 0.0039 pN/nm given that the probe is only 14 nm from the substrate, almost identical to the trapping stiffness (0.0036 pN/nm) 10–20 s earlier when the surface was ~90 nm below the trap center.

4.3.3. MLE trial functions and super-resolution

In verifying the optical trap to be a perfect harmonic 3D spring at ~90 nm from a surface, we showed the equilibrium distributions of free probe vertical and transverse positions in Fig. 4.3 to be independent Gaussians, each governed by a spring constant and all with a minimum at a common center position. Thus, postulating the trapping potential to remain harmonic when close to a steric substrate, we assume that the appropriate trial function for super-resolving equilibrium distributions of free probe heights above a steric boundary will also be Gaussian in shape. In this case, however, the Gaussian will be truncated precipitously at one side by the surface. Idealized as such, the entropy restriction is predicted to induce a small long-range steric force that shifts the Gaussian center outward from the original trap center. As shown in Appendix A, normalization of the truncated probability density establishes the following "canonical partition" function Z_{eq} that quantifies the change in free energy driven by the entropy restriction:

$$\begin{aligned} \rho(z) &= \tfrac{H(z_W)}{Z_{eq}} \exp\left\{-\tfrac{(z-b)^2}{2\sigma^2}\right\}, \\ Z_{eq} &= \tfrac{2\pi\sigma^2}{2}\left(1 + erf\left\{\tfrac{-z_W+b}{\sqrt{2\sigma^2}}\right\}\right) \end{aligned} \tag{4.4}$$

where z_w is surface position relative to the original trap center at zero, $H(Z_W)$ is a Heaviside (0–1 step) function, and σ^2 is the variance. First law conservation of energy requires the differential change in free energy of the probe to equal the differential work of its displacement in the trap at equilibrium. This defines a long-range steric force, $f \equiv \kappa_{OT} b$, *pushing* the probe equilibrium position $b(z_w)$ outward under encroachment by the substrate.

The trail distribution given by Eq. (4.4) is then convolved with a random tracking error Gaussian, $\sim \exp[-(z-z')^2/2\sigma_{err}^2]$, to define the following trial function used to fit the experimental data:

$$\begin{aligned} \rho^{fit}(z) &= \tfrac{\rho^*(z)}{\int d\xi \rho^*(\xi)} \\ \rho^*(z) &= \left(G(\sigma_{err}, z-z') * H(z_W) \exp\left\{-\tfrac{(z'-b)^2}{2\sigma_{obs}^2}\right\}\right) \end{aligned} \tag{4.5}$$

Because the shift $b(z_w)$ in trap equilibrium position depends on location of the substrate relative to the original trap center, the MLE search involves iterations on two fitting parameters: the variance σ^2, and the wall position z_w.

5. Live cell demonstrations

As prototype cell targets for demonstrations, we have chosen motile leukocytic cells spreading on coverglass substrates. Analogous to the behavior of many soft deformable cells involved in early tissue development and in immune system functions, the prominent characteristic of leukocytes is that they selectively adhere to – and migrate through – the endothelial boundary of vessel walls when triggered by stimuli. Although multiple sets of adhesion molecules are involved in integrin interactions, the super Ig-family ligands play the most prominent roles in firm adhesion of the cells and their subsequent emigration into tissues [10–11]. Integrins comprise a large family of heterodimers and exist in different conformational states correlating with imperceptible – to ultra strong – adhesion depending on activation. Moreover, in many biological processes, changes in integrin conformation and adhesiveness are initiated through "outside-in" and "inside-out" signaling [12]. The directional feedback is triggered in the first case by ligand binding, and in the second case by chemokine or cytokine stimulation.

We have employed immortalized human tumor lymphocytes called Jurkats taken from culture to model leukocyte spreading and the important receptor dynamics associated with integrin ligation. For simple demonstration of contour imaging, we used a probe passivated as described in Section 3.2. More challenging by comparison, we have conjugated the probe with recombinant fragments of fibronectin (FN296) to demonstrate the fast telemetry of ligand–receptor binding events and the kinematic movements of binding sites subsequent to receptor ligation – in this case, VLA-4 (α_4 β_1) integrin.

5.1. Topographic imaging

Imaging the height profile of a thin transparent cell lamella or filopodia is perhaps the simplest application of the method. Gently brushing the lamella surface past a passivated probe, we are able to map out the coarse details of the local cell topology as shown in Fig. 5.1 (movie S1). The approach is to position the lamella surface under a levitated probe and elevate the surface to gently compress the diffuse downward fluctuations of the probe. Then the lamella is translated laterally at a constant speed allowing the probe to gently move up/down over the surface topography. If desired, the lateral probe deflections along the traverse can also provide a scan of the probe-surface friction or a map of very weak probe-surface adhesion (*vis a vis* strong interactions that capture the probe). However, the lateral resolution in any transverse scan is limited when reported by a 500-nm radius probe. Despite such a limitation, the value of the approach is its capability to image the topographies of very soft live surfaces with impingement forces of a few fN. One such surface is the spreading Jurkat lamella shown in Fig. 5.1A, which was scanned by a $\sim$1 μm diameter probe held in a 100 mW trap ($\kappa^n_{OT} \sim 0.008\,\mathrm{pN/nm}$). Pulled over finger-like projections and intervening valleys, the probe traverse is shown highlighted by a white-bordered rectangle in Fig. 5.1A. With the probe drawn above to scale, the scan height profile (black/red curve) is shown plotted in Fig. 5.1B at low magnification along the traverse.

Enlarged twenty-fold in Fig. 5.1C, the height profile in 3D reveals the dense probe fluctuations that accompany the traverse (±10 nm SD including random tracking errors). The magnified profile of heights shows the topography of prominent filopodia traversed in the scan, which rise $\sim$150 nm above – and between – deep depressions 1000 nm apart. Although not examined, these filopodia grow and shrink as cells move over a substrate. Most intriguing is the "fuzz" of probe fluctuations encasing the profile which, though dense, is significantly smaller than the spread in vertical positions expected for the soft trap near a smooth steric boundary (±30 nm SD, cf. Section 4.3). This suggests that the probe fluctuations represent a profile of cell-interface compliance which, if thermally distributed, would characterize apparent spring constants, $\kappa_B\mathrm{T/SD2} \sim 0.05\,\mathrm{pN/nm}$ (when corrected for random tracking errors). Although too complicated to be discussed here, we expect such a profile to characterize confinement of the probe against a rough and weakly deformable surface by variable height-dependent impingement forces along the contour, i.e. $f_{imp} \sim 0.1 - 1\,\mathrm{pN}$.

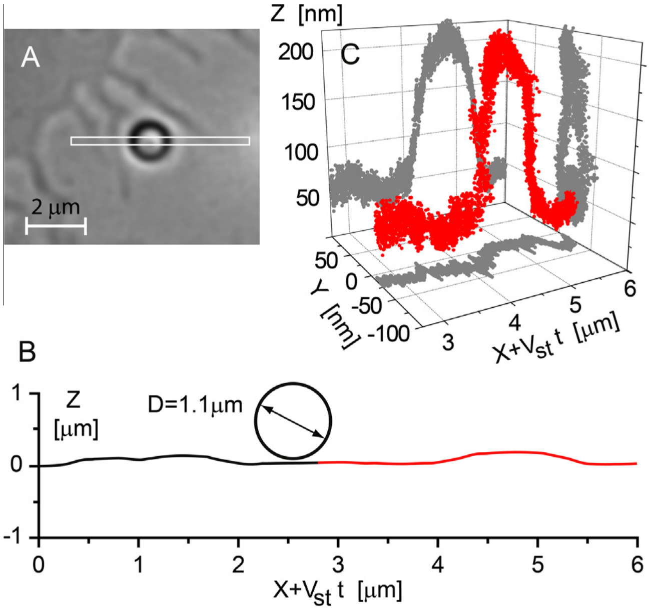

Fig. 5.1. Topography of a Jurkat cell lamella imaged in a lateral traverse past the probe. (A) Bright-field image of the Jurkat cell periphery revealing a lamella segment with several fjord-like invaginations between finger-like filopodia. The probe sphere $\sim$1 μm in diameter can be seen near the image center. The long white line (open) rectangle highlights the probe traverse. In the traverse, the coverglass substrate and spread cell were moved right to left at Vs = 50 nm/s. (B) The low magnification height profile along the traverse (black/red line) with the probe drawn above to scale. The raised regions correspond to the prominent cell filopodia extending diagonally outward in A. (C) The height profile magnified twenty-fold is plotted in 3-D for the segment highlighted red in panel B. The "fuzz" bordering the profile is the probe fluctuation distribution (±10 nm SD including random tracking errors). Much more tightly confined than in the soft vertical trap, the probe fluctuations provide an image of the cell-interface stiffness along the traverse under impingement forces over the range 0.1–1pN.

5.2. Ligand–receptor binding and lamella dynamics

Much more complex than imaging passive surfaces, here we show examples of nanoimaging leukocyte lamellae using a ligand-coated probe that are interrupted by dramatic collapses of the free probe fluctuations signaling probe ligation to a cell-surface integrin. When a probe ligand is captured by a surface receptor, fluctuations of the probe are almost completely suppressed by the short linkage to the nearby cell surface, which is a rough and changing steric boundary covered by a thick glycocalyx. Even though strongly confined and unaffected by the vertical trapping potential, the distributions of probe positions can be used to track the location defining a binding site and reveal unexpected cytoskeletal contractions triggered by the binding event. Although the binding events are random, we will demonstrate an effective off-line method to super-resolve of the kinematics to provide an assay for how a ligand-integrin complex moves and flexes throughout its brief existence.

5.2.1. Bare kinematics of ligation in 3-D

Fig. 5.2A shows the vertical probe positions during an initialization cycle of surface referencing that ends with the trap center about 50 nm above a Jurkat cell lamella. While continuing to track probe positions as shown in Fig. 5.2A, the probe positions suddenly collapse to an elevation close to the cell surface at 5.5 s, marking the onset of ligation. The complex persists for about 4 s until the ligand precipitously dissociates from the integrin allowing diffuse fluctuations to quickly re-emerge. Quite unexpected and without disrupting the complex, the surface retracts sharply downward about 2.5 s after the initial ligation and then returns to the prior elevation ~1 s later, remaining near there until dissociation about 2 s later (movie S2).

The trajectory of probe movements in 3D is shown in Fig. 5.2B, revealing the fine details of the surface retraction event. The solid (color-coded) trajectory is a 5-point moving average of the probe positions, which yields a single value for each time frame. The 3D trajectory starts at the onset of the color-coded section of the height trace in Fig. 5.2A. The trajectory starts and ends with regions that identify positions before the ligation event and after dissociation that appear in navy. The intervening regions during ligation are coded as follows: the initial and final ligation phases, ~5.5–8 s and ~8.8–9.5 s, are coded green; the surface retraction event is coded red. Plotted as closed circles and color-coded in the same way are the projections of the position trace onto the XY and YZ planes defining the 3D space.

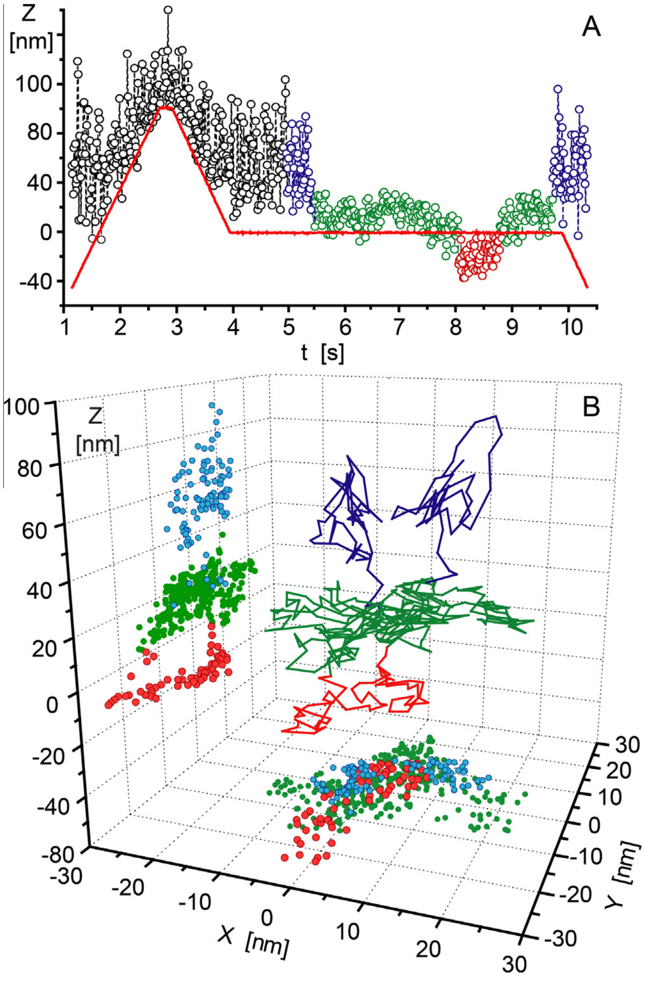

Fig. 5.2. A time trace of probe height positions above a cell lamella that begins with an initialization cycle (red line *wedge*) to establish the reference height for the lamella boundary and then continues at a fixed elevation ~50 nm below the trap center. Probe height positions imaged at the fixed elevation are shown color-coded in A to identify and mark the random formation and release of a ligand-integrin bond (as well as an intervening downward retraction of the lamella surface and complex). Signified by sudden collapse of large probe fluctuations, ligation to the integrin then persists ~4 s until dissociation. (B) The continuous 5-point moving average of positions in 3D encompassing capture of the probe by a cell surface integrin. Projected on bounding planes of the 3D space are the probe positions (color-coded to match corresponding segments in the trace A).

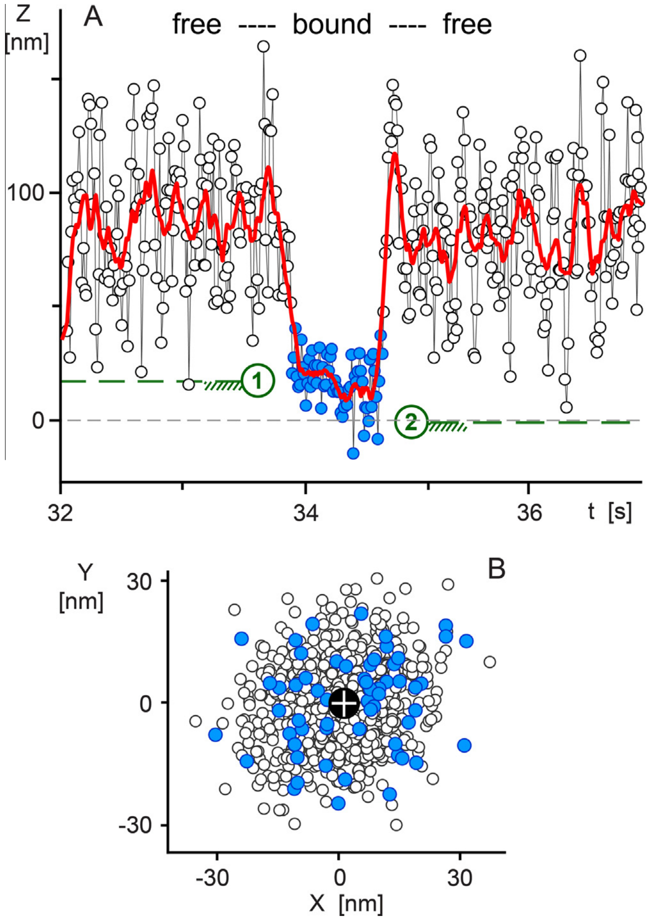

Fig. 5.3. Probe heights relative to the initial surface referencing trajectory performed 32 s earlier (red base line). (A) Bare height trace from tracking as a function of time (open circles). The red trace is a 10-point moving time-average of the bare height trace. The abrupt collapse of the probe heights at ~33.9 s signifies the onset of ligation and probe capture (positions marked by blue circles). The re-emergence of diffuse free probe fluctuations at ~34.7 s signifies dissociation. Like the image trace in Fig. 5.2, the lamella surface and ligand-integrin complex are retracted sharply downward ~0.3 s after the initial ligation and remain there until the complex dissociates ~0.5 s later. Shown by supported green lines are MLE predictions of the steric boundary references determined over 2 s periods before ("1" 17 nm) – and after ("2" −1 nm) – probe capture. (B) Projections of the probe positions on the XY plane. Shown by open gray circles are positions prior to – and after – probe capture. Superposed are the lateral positions (blue circles) of when bound.

5.2.2. Displacements of the receptor binding site relative to lamella structure

We end our nanoimaging chapter by demonstrating an off-line analysis of probe positions that significantly improves determination of the lamella surface boundary and relative distance to a site of ligand-integrin binding. Not only detailing how a ligand-integrin complex moves and flexes throughout its brief existence, the post-processing exposes how the cell cytostructure occasionally reacts to ligation of a single integrin – a response presumably triggered by a chemical signalling pathway inside the cell. For this demonstration (shown in Fig. 5.3), we have selected a binding event with short lifetime (<1 s) revealing a precipitous retraction of the binding site by the cell cytoskeleton prior to dissociation.

Analyzing each 2 s period of free probe fluctuations, we determined two height references for the lamella boundary, which are identified by green markers "1" and "2" in Fig. 5.3, have been determined using MLE fits matched to all free probe heights given Gaussian trial functions truncated by steric boundaries and convolved with the random tracking errors.

Although preceded and followed by periods with more than 200 free probe fluctuations in Fig. 5.3, only ~30 positions characterize bound state positions observed during the each of the two segments defined by the cytoskeletal retraction, thereby posing a significant obstacle to super- resolution. Hence, to super-resolve kinematics of the cell surface and ligand–receptor binding positions during a brief (~1 s or less) period of ligation, we employ a simple approach that first establishes reference heights for the stationary cell lamella surface before – and – after the binding event and then uses these positions to characterize relative movements of the binding site at the beginning and end of the ligation period. Performed in this way, we take advantage of the free probe motions and the MLE fitting methods described in 4.3.3 to determine surface elevations that are contemporary with the internal dynamics of the binding event. In Fig. 5.3, the red base line at 0 nm shows the boundary elevation determined by the initial height referencing cycle performed 32 s earlier. By comparison, analysis of the 2 s period prior to probe capture shows that the lamella boundary has shifted upward by 17 nm (the green marker labeled "1" in Fig. 5.3). Not unexpected, the slow movements of a crawling cell often shift the lamella boundary significantly from an initial reference elevation determined a long time before a binding event. On the other hand, what occasionally shifts the boundary more precipitously is the type of cytoskeletal retraction event shown previously in Fig. 5.2A and again in Fig. 5.3 by analysis of the 2 s period following ligand dissociation (cf. green marker labeled "2" at −1 nm).

Cut out from Fig. 5.3A for the period 33.9–34.7 s and magnified in Fig. 5.4, we have used a moving-average height trajectory to define the binding site location. Approximated as two stationary levels, a mean value of 24 nm defines the starting level over 0.3 s, then drops to a mean value of 14 nm over the remaining 0.5 s (means with standard errors ±1 nm). By Compared to the two boundary references (17 nm and −1 nm), we then determine the relative distances (exposed lengths) between the binding site location and steric boundary to be 7 nm and 15 nm respectively, suggesting ~8 nm extension of the separation.

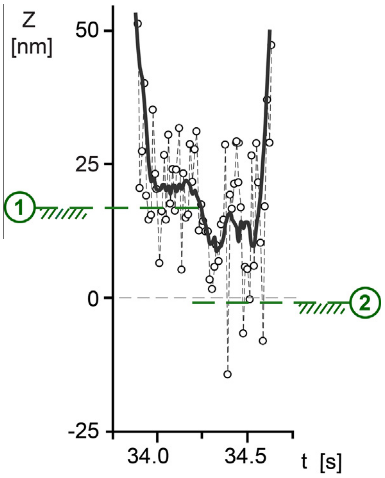

Fig. 5.4. Binding site dynamics with contemporary surface referencing. Probe heights are plotted as a function of time spanning the onset of integrin ligation until dissociation. Open circles are bare height positions from tracking. The solid black trajectory is a 10-point moving average of the bare height trace. Shown by supported green lines are MLE predictions of the steric boundary references determined over 2 s periods before ("1") – and after ("2") – the binding event. Compared to the two boundary references (17 nm and −1 nm), the relative distances between the binding site location and steric boundary are found to increase from 7 nm to 15 nm upon cytoskeletal retraction.

This last demonstration again highlights the enhanced fidelity of free probe movements close to a surface and the unexpected benefit of blur suppression by hydrodynamic retardation close to a cell surface. Yet, at the same, the demonstration also exposes the inadequacy of imaging at ~100 fps when bound to the surface for brief periods, which brings with it increased succeptibility to motion blur as the consequence of more confined fluctuations. Fortunately, there are current camera systems available that will provide the same tracking precision using 10× or faster image-capture rates. We are presently interfacing a new camera with this capability to our imaging system.

Acknowledgements

This work was supported by USPHS NIH grants R01 HL65333 and R01 AI044902. The authors acknowledge the important contributions by our long time University of British Columbia colleagues Andrew Leung and Koji Kinoshita to the developments of probe linkage chemistry, cell culture protocols, and instrument assembly. The authors also acknowledge the gracious hospitality of Professor Kevin Malloy at the University of New Mexico, in whose lab the authors were encouraged to set up and prototype the imaging instrument using equipment from the EE lab at Boston University.

Appendix A. Statistical thermodynamics and entropic repulsion

When thermodynamically equilibrated, we demonstrated in Fig. 4.3 that the optical trap can be characterized in 3D by independent transverse and vertical harmonic springs (spring constants $k^i_{OT} = \partial^2 E/\partial x_i^2$) over the stable region bordered by the energy barriers defining escape. Viewed in the context of probe height fluctuations, the substrate below the probe defines an impenetrable barrier to its downward movements. In reality, this barrier has structure (roughness) and interacts with other objects at long range through distance-dependent fields (e.g. electrostatic, van der Waals, depletion, etc.). However, in aqueous environments containing high salt concentrations and given the modest differences in dielectric properties of cell membrane materials relative to water, the long-range fields usually fall off quite rapidly from the membrane surface (within 1–2 nm), which neglects possible formation of weakly-specific ionic or hydrogen bonds. If non-adhesive, the barrier to free probe height fluctuations lies somewhere within the interfacial structure, which as schematized in Fig. 2 can be 10–20 nm or more in thickness for a cell. Even so, our live cell demonstrations in Section 5.2 show that this glycocalyx structure is quite stiff and thus appears rigid to free probe movements in a soft vertical trapping field. Thus, we have used a rigid steric boundary ("wall" at z_w) to represent the elevation of a live or inert substrate relative to the probe equilibrium state in a trap far from boundaries. However, entropy confinement by proximity to a steric boundary pushes the probe position at equilibrium away from the boundary thereby establishing a new trap center (minimum).

To quantify the shift in equilibrium position, we assume that the optical trapping field remains harmonic and unperturbed by proximity to the steric boundary (as verified in Section 4.3.2). Thus, the distribution of free probe height fluctuations remains Gaussian yet is truncated to zero precipitously at the steric boundary z_w as given by the following un-normalized probability density:

$$\begin{cases} \rho(z > z_w, b) \sim \exp\{-(z-b)^2/(2\sigma^2)\} \\ \rho(z \leqslant z_w, b) = 0 \end{cases} \tag{A1}$$

where $\sigma^2 = k_BT/\kappa_{OT}$ and b is the location of the Gaussian peak relative to the original trap minimum at $z = 0$.

Appendix B. Boltzmann thermodynamics

Determining the factor that normalizes the truncated Gaussian in (A1), we obtain the canonical partition function Z_{eq} defining the free energy relative to a state where the boundary is at $-\infty$:

$$\begin{aligned} \Delta F &= -k_BT\left[\ln Z_{eq} - \ln\sqrt{2\pi\sigma^2}\right] \\ Z_{eq} &= \int_{-z_w+b}^{\infty} dy \exp\left\{\frac{-y^2}{2\sigma^2}\right\} = \frac{\sqrt{2\pi\sigma^2}}{2}\left[1 + erf\left(\frac{-z_w+b}{\sqrt{2\sigma^2}}\right)\right] \end{aligned} \tag{A2}$$

First law conservation of energy requires the differential change in free energy of the probe to equal the differential work of its displacement in the trap at equilibrium. This defines a long-range steric force, $f \equiv \kappa_{OT}b$, *pushing* the probe equilibrium position $b(z_w)$ outward under encroachment by the substrate. Thus, minimizing the free energy plus the trapping energy (i.e. maximizing the entropy), we determine the equilibrium state of the probe:

$$\begin{aligned} &\delta F + \kappa_{OT} b \delta b = 0 \\ &\frac{\partial F}{\partial b} = -\kappa_{OT} b \end{aligned} \tag{A3}$$

To find the new trap equilibrium position b, we then solve the following transcendental equation:

$$\begin{aligned} \frac{\partial F}{\partial b} &= -k_BT\frac{\partial \ln Z_{eq}}{\partial b} = -\kappa_{OT} b \\ &= \frac{-k_BT}{1+erf\left[(b-z_w)/\sqrt{2\sigma^2}\right]}\frac{\partial}{\partial b} erf\left(\frac{b-z_w}{\sqrt{2\sigma^2}}\right). \end{aligned} \tag{A4}$$

thereby revealing the steric repulsion driven by entropic confinement (Fig. 6),

$$\begin{aligned} f_{steric} &= \kappa_{OT} b = \sqrt{\frac{2k_BT\kappa_{OT}}{\pi}} \\ &\times \frac{1}{1+erf\left[(b-z_w)/\sqrt{2k_BT/\kappa_{OT}}\right]} \exp\left(\frac{-(z_w-b)^2}{2k_BT/\kappa_{OT}}\right) \end{aligned} \tag{A5}$$

and the shift in trap position,

$$b = \sqrt{\frac{2\sigma^2}{\pi}}\left(1 + erf\left\{\frac{b-z_w}{\sqrt{2\sigma^2}}\right\}\right)^{-1} \exp\left\{-\frac{(b-z_w)^2}{2\sigma^2}\right\}. \tag{A6}$$

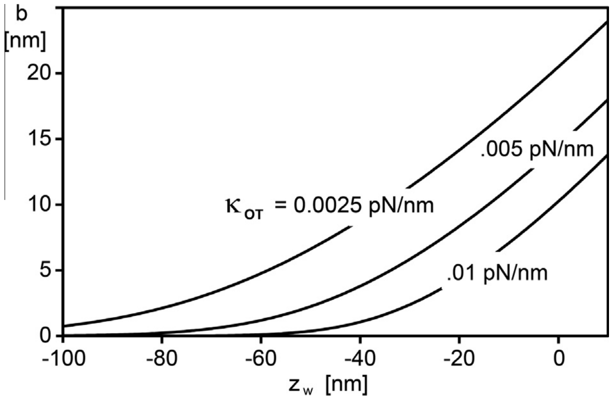

Fig. 6. Equilibrium shift b in trap center is shown plotted as a function of the wall position z_w for three values of the OT spring constant.

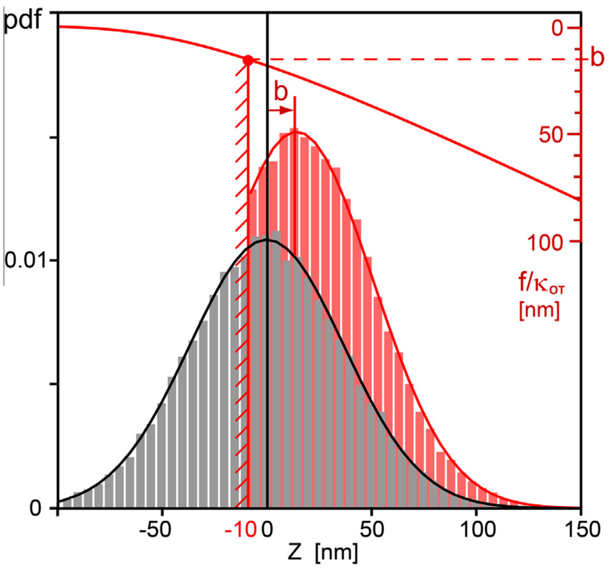

Fig. 7. Gray histogram: simulated data of a 1 μm probe in a κ_{OT} = 0.003 pN/nm trap for a case when the steric wall is placed at $z_w = -500$ nm. In this case the steric shift is negligible, and can be used to define the thermodynamic reference described above for the trapping potential (i.e. the peak of the normalized Gaussian MLE fit, black line). When the wall is moved close to the trap center, the entropic repulsion displaces the trap minimum outward from the origin. For $z_w = -10$ nm, a shift b = 15nm is found from the MLE fit shown by the solid red line. The resulting equilibrium distribution of the simulated states (red histogram) is fitted with the function given by Eq. 4.4 of the main text. Both the normalized Gaussian fits (to red and grey histograms) return σ = 37nm.

Appendix C. Steric repulsion in the SMC simulation

For each elevation of the steric wall in a time trajectory of displacements, a steric shift is calculated from Eq. A6 and is used to define the equilibrium condition guiding the Markovian Langevin dynamics. Fig. 7 shows schematically the calculation of such shift and the resulting equilibrium distributions from SMC simulation.

Appendix D. Supplementary data

Supplementary data associated with this article can be found, in the online version, at http://dx.doi.org/10.1016/j.ymeth.2013.03.038.

References

[1] B. Huang, H. Babcock, X. Zhuang, Cell 143 (2010) 1047–1058.
[2] W.J. Greenleaf, M.T. Woodside, S.M. Block, Annu. Rev. Biophys. Biomol. Struct. 36 (2007) 171–190.
[3] F. Coussen, D. Choquet, M.P. Sheetz, H.P. Erickson, J. Cell Sci. 115 (2002) 2581–2590.
[4] G. Jiang, G. Giannone, D.R. Critchley, E. Fukumoto, M.P. Sheetz, Nature 424 (2003) 334–337.
[5] V. Heinrich, W.P. Wong, K. Halvorsen, E. Evans, Langmuir 24 (2008) 1194–1203.
[6] E. Evans, K. Halvorsen, K. Kinoshita, W.P. Wong, in: P. Hinterdorfer, A. van Oijen (Eds.), Handbook of Single-Molecule Biophysics, Springer Science+Business, Media, 2009, pp. 571–589.
[7] W.P. Wong, K. Halvorsen, Optics Express 14 (2006) 12517–12531.
[8] A.J. Goldman, R.G. Cox, H. Brenner, Chem. Eng. Sci. 22 (1967) 637–651.
[9] P.J. Rossky, J.D. Doll, H.L. Friedman, J. Chem. Phys. 69 (1978) 4628–4633.
[10] R. Zaidel-Bar, S. Itzkovitz, A. Ma'ayan, R. Iyengar, B. Geiger, Nat. Cell Biol. 9 (2007) (2007) 858–867.
[11] R.O. Hynes, R.O., Cell 110 (2002) (2002) 673–687.
[12] B.H. Luo, C.V. Carman, T.A. Springer, Annu. Rev. Immunol. 25 (2007) 619–647.